



Inverse design of compact multimode cavity couplers

WEILIANG JIN,¹ SEAN MOLESKY,¹ ZIN LIN,² KAI-MEI C. FU,³ AND ALEJANDRO W. RODRIGUEZ^{1,*}

¹*Department of Electrical Engineering, Princeton University, Princeton, NJ 08544, USA*

²*John A. Paulson School of Engineering and Applied Sciences, Harvard University, Cambridge, MA 02138, USA*

³*Department of Physics University of Washington, Seattle, WA 98195, USA*

*arod@princeton.edu

Abstract: Efficient coupling between on-chip sources and cavities plays a key role in silicon photonics. However, despite the importance of this basic functionality, there are few systematic design tools to simultaneously control coupling between multiple modes in a compact resonator and a single waveguide. Here, we propose a large-scale adjoint optimization approach to produce wavelength-scale waveguide–cavity couplers operating over tunable and broad frequency bands. We numerically demonstrate couplers discovered by this method that can achieve critical, or nearly critical, coupling between multi-ring cavities and a single waveguide at up to six widely separated wavelengths spanning the 560–1500 nm range of interest for on-chip nonlinear optical devices.

© 2018 Optical Society of America under the terms of the [OSA Open Access Publishing Agreement](#)

1. Introduction

Practical limitations of nanophotonics for broadband applications are seldom known and highly context specific [1–3]. In single frequency problems, traditional design principles based on index-guiding, Bragg scattering, and material resonances offer clear trade offs, e.g., spatial confinement for radiative losses, or peak performance for bandwidth. But, in many multi-frequency problems, including nonlinear optics [4,5], imaging [6,7], radiative heat transfer [8,9], and optical networks [10], the number of parameters that influence performance is simply too large to treat completely using analytic methods or hand-designed geometries, and it is often unclear what level of performance can be attained. Over the last two decades, this challenge has spurred the development of large-scale optimization (inverse) techniques to assist in the design process with promising early returns [11–13]. Yet, in many technically important areas only preliminary investigations have been made [14]. Specifically, the power required to attain efficient nonlinear frequency conversion processes is known to decrease with increasing spatial confinement, so long as the overlap of the participating modes can be controlled [15]. To take full advantage of this effect, we have recently proposed several optimized resonators to enhance nonlinear second harmonic and difference frequency generation in wavelength-scale volumes [16,17]. To operate on-chip, each mode in a device making use of these cavities must be coupled to a source or detector in a controlled way; and until presently, we have not addressed how this can be done. Using a typical evanescent scheme, tuning the gap separation to control evanescent overlap between the waveguide and cavity [18], realization of high efficiency devices using these cavities, and similar future designs, may be difficult. Beyond the issues of layout intricacy, bending loss [19,20], and waveguide crosstalk [21,22] that would be introduced by requiring multiple waveguides to intersect in a wavelength-scale area, modes in the best performing cavities designs may be tightly confined to the core [17], precluding the possibility of achieving critical or over coupling by simply decreasing the separation.

This problem of efficiently coupling light between sources and predefined volumes appears in

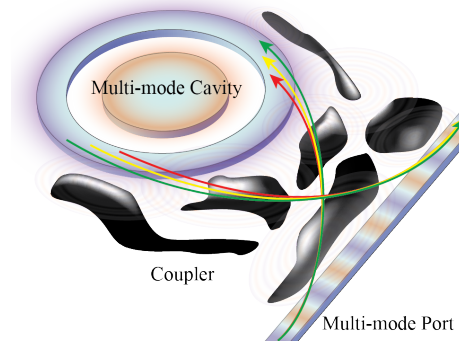


Fig. 1. **Schematic of a general cavity coupler:** A compact scatter (black region) acts as a coupler between a wavelength-scale, multimode cavity and a multimode port (waveguide). The design freedom of the scatter enables controllable coupling between the two devices at several wavelengths (red, yellow, and green arrows).

many branches of nanophotonics. For instance, it is the defining goal of wide-area absorbers—surfaces that can perfectly absorb a wide range of incident propagating waves. Broadly, the main approach in this setting is to create structures supporting many resonances in order to tune the radiative and absorptive decay rates in each scattering channel [23]. This behaviour can be introduced in a wide variety of ways, including adiabatic tapers [24, 25], metasurfaces [26, 27], epsilon-near-zero thin films [28, 29], chirped gratings [30, 31], multi-resonant photonic crystals [32], and more recently, unintuitive structures obtained via inverse design [33–35]. A similar objective also appears in the context of free-space to on-chip couplers, with the primary aim being to reduce losses, i.e. reflections, of light incident on a on-chip device from either a fiber or free space. Rate matching is more difficult to implement in these situations, as any signal decay (e.g. material absorption in the coupling region) reduces performance; and common approaches based on adiabatic tapers lead to couplers that are several wavelengths long and are only typically designed to operate over narrow, selective bands [36–39]. Based on motivations similar to those of this present study, there is a current push to exploit inverse design [40, 41], metasurface concepts [42–44], and chaotic deformations [45] in this area. Likewise, a need to control coupling arises between on-chip devices, including filters, rectifiers, multiplexers, and frequency converters. In these situations, the usual goal is to efficiently couple two or more separately designed devices in the smallest possible footprint. Again, much in the spirit of the results presented here, within the past few years inverse design approaches have started to be applied in this setting, leading to experimental demonstrations of compact wavelength-division multiplexers operating over several far-apart wavelengths [46, 47].

In this paper, we present a large-scale optimization algorithm for designing compact on-chip devices that efficiently couple light consisting of multiple, widely separated wavelengths from a single waveguide into a wavelength-scale multi-resonant cavity. Motivated by practical problems in nonlinear optics, we pursue three illustrative examples: compact multi-resonant cavities with resonant features mimicking those used for second-harmonic, sum-frequency, and frequency comb generation. In each situations, we demonstrate either total or near total critical coupling.

2. Formulation

Our conception of the coupling problem is depicted in Fig. 1. Starting from an isolated cavity supporting N resonances with frequencies ω_i and radiative lifetimes $Q_{i,r}^0$, $i = \{1, 2, \dots, N\}$, we aim to design a wavelength-scale device that tunes the external coupling rate of each mode to a single nearby waveguide to any desired value. That is, we seek to independently control the dimensionless coupling quality factor $Q_{i,c}$ of every individual mode of a given set. Generically,

the presence of a coupler or a nearby waveguide can significantly alter the radiative decay of an isolated cavity modes, either enhancing or degrading temporal confinement. To ensure that the resonant features of the cavity are not destroyed by the coupler, we simultaneously constrain $Q_{i,r}^0 \leq \alpha_i Q_{i,r}$, with $Q_{i,r}$ denoting the radiative quality factor of the cavity in the presence of the waveguide and coupler, and α_i an adjustable scale factor. Based on this description, a structure for any desired collection of coupling characteristics is discoverable using a gradient adjoint-variable topology optimization approach [48] that seeks to solve the minimax problem,

$$\begin{aligned} & \min_{\{\bar{\epsilon}\}} \mathcal{F}(\mathbf{E}, \bar{\epsilon}) \\ & \text{s.t. } \{\mathcal{G}_i(\mathbf{E}, \bar{\epsilon}) \leq 0\}, i = 1, 2, \dots, N \\ & \epsilon_{\text{sub}} \leq \bar{\epsilon} \leq \epsilon_{\text{st}}, \end{aligned} \quad (1)$$

where

$$\begin{aligned} \mathcal{F}(\mathbf{E}, \bar{\epsilon}) &= \max_{i=1}^N [Q_{i,c}(\mathbf{E}, \bar{\epsilon}) - \xi_i Q_{i,r}(\mathbf{E}, \bar{\epsilon})]^2 \\ \mathcal{G}_i(\mathbf{E}, \bar{\epsilon}) &= Q_{i,r}^0 - \alpha_i Q_{i,r}(\mathbf{E}, \bar{\epsilon}), \end{aligned} \quad (2)$$

with ξ_i denoting the target ratio of $Q_{i,c}/Q_{i,r}$. In this method, the dielectric permittivity at every spatial point inside the coupling region, $\{\bar{\epsilon}\}$, is as a continuous degree of freedom, bounded by the substrate ϵ_{sub} and structure ϵ_{st} materials. (To produce binary, smooth, fabricable systems additional regularization and filter projection steps are applied in conjunction with this base algorithm [49].) In order to circumvent numerical issues associated with optimizations of electromagnetic eigenvalues [48], each Q is computed by solving a set of scattering problems. This makes both the objective \mathcal{F} and constraints \mathcal{G}_i explicit functions of the electric field \mathbf{E} , computed as the solution of the steady-state equation $[\nabla \times \frac{1}{\mu} \nabla \times - \omega_i^2 \epsilon(\omega_i, \mathbf{r})] \mathbf{E}(\omega_i, \mathbf{r}) = i\omega \mathbf{J}(\omega_i, \mathbf{r})$. To setup this problem, electric current sources, the duals $\mathbf{J}(\omega_i) \propto \text{Re}[\epsilon(\omega_i)] \mathbf{E}^*(\omega_i)$ of the modes in the energy norm [50], are first calculated (without the waveguide and coupler) at each individual frequency. The waveguide and coupler are then added, and the field quantities of interest determined: the electromagnetic energy density inside the cavity volume, $U_i = \frac{1}{2} \int_V dV \epsilon(\omega_i, \mathbf{r}) |\mathbf{E}(\omega_i, \mathbf{r})|^2$, and the Poynting flux into the waveguide and radiated into vacuum, $P_i = \frac{1}{2} \int_{\Sigma} d\mathbf{s} \cdot \text{Re}[\mathbf{E}(\omega_i, \mathbf{r}) \times \mathbf{H}(\omega_i, \mathbf{r})]$, with Σ denoting the corresponding flux surfaces. The radiative and coupling lifetimes $Q_{i,c(r)} = \omega_i U_i / P_{i,c(r)}$ are then used to evaluate \mathcal{F} and \mathcal{G}_i .

In many applications of interest, one of two coupling characteristics are often desired: over coupling [51, 52], minimizing unwanted losses and increasing energy efficiency, or critical coupling, maximizing field amplitudes in the cavity [16]. For cavities designed to enhance nonlinear frequency conversion, such as the illustrative examples considered below, maximum power conversion occurs under critical coupling, $\xi_i = 1$, at each frequency. In such cases, the general scheme presented above can be simplified. When the cavity is pumped from a single channel with power P^{in} , the energy in the cavity is related to the quality factors by [53]

$$\frac{\omega_i U_i}{P_i^{\text{in}}} = \frac{4 Q_{i,r}}{2 + Q_{i,r}/Q_{i,c} + Q_{i,c}/Q_{i,r}}, \quad (3)$$

reaching a relative maximum of $Q_{i,r}$ as the system moves toward critical coupling ($\xi_i \rightarrow 1$). Technically, (3) is only applicable to unidirectional couplers, i.e. when each cavity mode couples only to one port (direction) of the waveguide. (A simple example of a unidirectional coupler is the usual waveguide–ring resonator system, where the direction of coupling is constrained by momentum conservation [54].) However, as the introduction of any additional coupling channel always reduces the energy stored in the cavity [53], in practice, there is no loss of

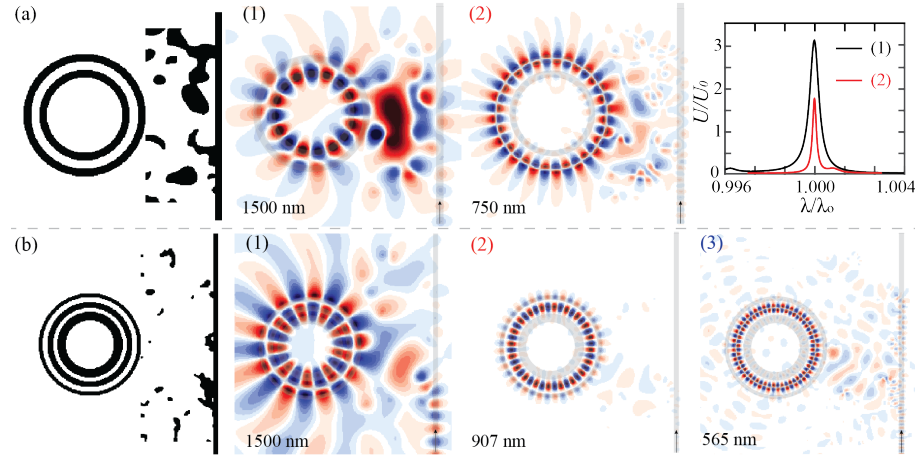


Fig. 2. **Nonlinear frequency conversion:** Optimized couplers for SHG (a) and SFG (b) showing critical coupling between multimode ring resonators and waveguides. All structures (black) are made of GaP, while the substrate (white) is assumed to be vacuum. For the SHG design, the width of the waveguide is 150 nm, the diameter of the outer ring $2.6 \mu\text{m}$, and the area of the designed coupling region $3.75 \mu\text{m} \times 1.5 \mu\text{m}$. The plot to the far right shows the energy spectrum inside the resonator near the fundamental and second-harmonic wavelengths $\lambda_{\{1,s\}} = \{1500, 750\} \text{ nm}$, with matched azimuthal wavenumbers $m_1 = 8$ and $m_s = 2m_1$, (black, red) normalized by U^0 . The middle figures show the TM-polarized electric fields at the respective wavelengths. The complete suppression of outgoing/transmitted power through the waveguide provides a visual confirmation of critical coupling. Similar results are seen for the SFG design, (b), with three modes $\lambda_{\{1,2,s\}} = \{1500, 907, 565\} \text{ nm}$, $m_{\{1,2,s\}} = \{9, 20, 28\}$, critically coupled between the cavity and waveguide. In this case, the width of the waveguide is 134 nm, the diameter of the outer ring $2.8 \mu\text{m}$, and the area of the coupling region is $5.4 \mu\text{m} \times 2 \mu\text{m}$. In both designs, the discovered structures are binary.

generality in considering this expression. By maximizing the energy in the cavity, the algorithm naturally proceeds towards unidirectional couplers, which in turn makes (3) an increasingly good approximation. Since the behavior of (3) is then ultimately equivalent to the more complicated (2), we are able to consider the simpler optimization problem,

$$\mathcal{F}'(\bar{\varepsilon}) = \max_{\bar{\varepsilon}} \left\{ \min_{i=1}^N \left[\frac{U_i(\mathbf{E}, \bar{\varepsilon})}{U_i^0} \right] \right\}. \quad (4)$$

Where the $U_i^0 = Q_{i,r}^{P_{i,\text{in}}} / \omega_i$ is an energy normalization factor given by the bare radiative lifetime. As a proof of concept, we consider two illustrative cavities designed to enhance two $\chi^{(2)}$ nonlinear processes: up-conversion of ω_1 and ω_2 to the summed frequency $\omega_s = \omega_1 + \omega_2$ (SFG), and second-harmonic generation (SHG) corresponding to degenerate SFG with $\omega_1 = \omega_2$. For these processes, the relative coupling rates largely dictate the achievable intensities in the cavity, and hence power requirements (in the undepleted regime [16]). Mathematically, this is captured by the figure of merit

$$\text{FOM} = |\beta|^2 \prod_{i=1,2,s} \frac{Q_{i,r}}{2 + Q_{i,r}/Q_{i,c} + Q_{i,c}/Q_{i,r}}, \quad (5)$$

with β denoting the overlap coefficient of the cavity fields, which to first order is not affected by the external waveguide or coupler. Like (3), (5) is maximized when all three modes achieve critical coupling, giving $\text{FOM}_{\text{max}} = |\beta|^2 Q_{1,r} Q_{2,r} Q_{s,r} / 64$.

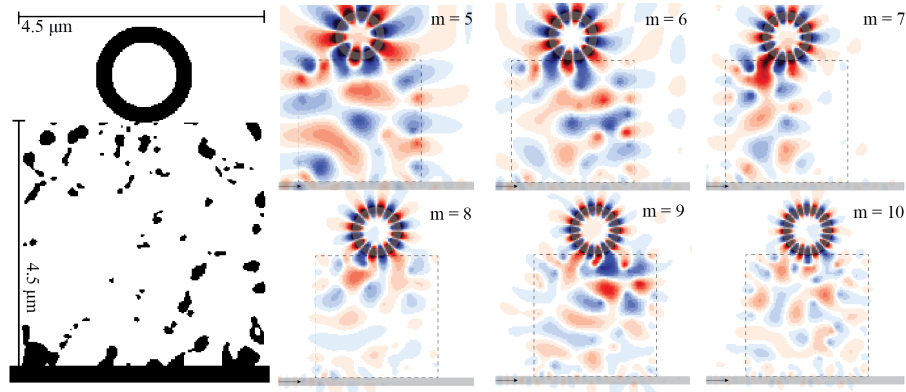


Fig. 3. **Frequency comb generation:** Optimized coupler for comb generation showing near critical coupling over 6 frequencies. The width of the waveguide is 300 nm, the diameter of the ring 1.8 μm , and the area of the designed coupling region 4.5 $\mu\text{m} \times 4.5 \mu\text{m}$. The figures show the TM-polarized electric field profiles at the respective azimuthal number $m = \{5 \rightarrow 10\}$, corresponding to frequencies $f = \{0.667 \rightarrow 1.157\} c/1.5 \mu\text{m}$, with equal spacing $\Delta f = 0.098 c/1.5 \mu\text{m}$.

3. Results

As a platform for testing our algorithm, similar to proposed wavelength-scale cavities for implementing nonlinear phenomena [17], we consider a two-dimensional system consisting of hand-designed multi-track ring-resonators supporting TM-polarized resonances (electric field out of the plane) of moderate radiative lifetimes $Q_{i,r}^0 \lesssim 10^5$, and a rectangular admissible coupler region covering the separation between the cavity and the waveguide. The size of this design region is determined on a case-by-case basis as a compromise between compactness and functionality. Starting from a base of 3.75 $\mu\text{m} \times 1.5 \mu\text{m}$ the size of the coupling region is increased whenever the algorithm is unable to find suitable coupling structures. To guide the algorithm towards more easily fabricable structures, the coupler is always seeded with connected, smooth dielectric profiles, i.e. a random ribbon. (For numerical accuracy, the grid resolution is chosen to be smaller than $\lambda/45$ for the smallest wavelength considered, ≈ 13 pixels per wavelength inside the highest index media.)

Our findings begin with the SHG and SFG systems depicted Fig. 2. For practical considerations, these simulations suppose a gallium phosphide material (including material dispersion) for all dielectric regions: the cavity, waveguide, and coupler. The initial SHG system is a two-track multi-ring supporting TM-polarized resonances at $\lambda_{\{1,s\}} = \{1500, 750\}$ nm, quality factors of $Q_{\{1,s\},r}^0 = \{1.4, 4.6\} \times 10^3$, with power coupled into the device through a narrow waveguide at a gap separation of $1.5\lambda_1$. (The azimuthal numbers of these modes satisfy the phase-matching condition $m_s = 2m_1 = 16$ for the (111) plane of a GaP crystal. Given a different nonlinear tensor and requisite polarizations, the phase-matching condition for m can be slightly different [55].) As indicated in the field profiles of Fig. 2(a), in the presence of the coupler each mode shows vanishing transmission and reflection ($\lesssim 2\%$), and large field amplitude inside the cavity. Quantitatively, Fig. 2(a) (rightmost) examines the energy spectrum inside the resonator channeled from the waveguide around $\lambda_{1,2}$, normalized by U_i^0 . After optimization, the cavity mode lifetime is more than doubled, with $Q_{\{1,s\},r}/Q_{\{1,s\},r}^0 = \{2.9, 2.2\}$. As expected, eigenmode analysis reveals the system to be totally asymmetric, with the cavity coupling exclusively to the lower waveguide (downwards propagation). The coupler is also observed to be both binary and smooth, having no feature smaller than 120 nm. Nearly identical results are seen for the triply resonant system (non-

degenerate SFG) illustrated in Fig. 2(b). Moving to a three-track cavity designed to support modes at $\lambda_{\{1,2,s\}} = \{1500, 907, 565\}$ nm, with $Q_{\{1,2,s\},r}^0 = \{640, 5.3 \times 10^4, 3.2 \times 10^4\}$, the algorithm is again able to realize critical coupling at all three wavelengths, resulting in transmission $\lesssim 1\%$. Cavity radiative lifetimes are also similarly enhanced, with $Q_{\{1,2,s\},r}/Q_{\{1,2,s\},r}^0 = \{2.2, 1.7, 3.1\}$. In either inverse design, the coupling mechanism is found to be more intricate than just the overlap of evanescent fields used for single wavelengths. This is most pointedly seen in (2) and (3) of Fig. 2(b), where over 99.5% of the energy density is in the cavity, yet critical coupling occurs at over two wavelength of separation due to the fields in the coupler. Moreover, for some cavity modes, even at a single wavelength, it would not be possible to achieve critical coupling using the evanescent tails of a waveguide mode. For example, due to its tight confinement to the inner ring, even if the waveguide is made to touch the cavity, it is not possible to couple to the mode displayed in Fig. 2(a.1) with better than 70% efficiency. (Reducing the waveguide cross-section offers no improvement due to the creation of phase mismatch.) Note that the radiative quality factors of the cavities we have designed are smaller than those typically considered for nonlinear processes. This choice was made primarily to test the algorithm in cases involving dissimilar waveguide and cavity mode profiles [56]. Nevertheless, we note that for equivalent nonlinear performance, larger overlaps β and smaller radiative lifetimes are often preferable to higher quality factors [16].

As a final benchmark, Fig. 3 demonstrates a system attaining near critical coupling at 6 frequencies (over an octave), a frequency comb with large tooth spacing. (A more practical frequency comb coupler, e.g. exhibiting critical coupling at over 100 frequencies, will be considered in future work.) In this case, we begin with a wavelength-scale ring resonator having unevenly distributed modes $m = \{5 \rightarrow 10\}$ at intervals $\Delta f = \{0.101, 0.099, 0.096, 0.098, 0.096\}c/1.5\mu\text{m}$, with $f_m = 2c/(4.5\mu\text{m}) + \sum_{i=0}^{m-5} \Delta f_i$. To simplify future comparisons, material dispersion is ignored and the cavity, waveguide and coupler are all assumed to have a constant permittivity of $\epsilon = 9.3514$. As opposed to our first two examples, where the modal resonance frequencies are fixed constraints, adding a degree of modularity to the total system design, here, we assume that the resonance frequencies must be tuned by the coupler. This conceptual shift requires some small modifications to stabilize the optimization algorithm. Namely, we now include an initial phase where the usual energy density objectives are replaced by field overlap integrals with the eigenmodes of the cavity $\int_V dV \text{Re} [\epsilon(\omega_i, \mathbf{r}) \mathbf{E}_m^*(\omega_i, \mathbf{r}) \cdot \mathbf{E}(\omega_i, \mathbf{r})]$, where the m subscript denotes the m^{th} mode of the bare cavity, and, as before, the integration is restricted to lie within the outermost material boundary of the cavity. The frequencies $\{\omega_i\}$ where these computations are carried out are initialized to match those of the bare cavity, and then slowly transitioned to the desired resonances, i.e. an evenly distributed set. The converged output of this procedure is effectively a new cavity having characteristics well-matched to the original coupling optimization algorithm. The coupler displayed in Fig. 3 achieves the desired wavelength tuning and critical-coupling functionality. The resonance frequency intervals are equally distributed as $\Delta f = 0.098c/1.5\mu\text{m}$, and good coupling (transmission and reflection below 15%) is visibly present in each of the field profile plots. Explicitly, the summed transmitted and reflected powers of are found to be $\{2\%, 5\%, 13\%, 2\%, 1\%, 4\%\}$. However, smaller minimal feature sizes, ≈ 15 nm, and a larger total footprint $4.5\mu\text{m} \times 4.5\mu\text{m}$ were required to achieve these effects. The number of iterations needed for this optimization was roughly the same as those of the previous examples, leading to approximately linearly scaling of the total computation time with the number of frequencies.

4. Concluding remarks

In summary, we have shown that, in two dimensions, inverse design provides a practical means of efficiently coupling light at multiple widely separated wavelengths from a single channel (a waveguide) into a compact, multimode cavity. Drawing from our recent work on the design of compact microcavities for high-efficiency nonlinear frequency conversion, we have successfully

treated suggestive examples for second-harmonic (SHG), sum-frequency (SFG), and frequency comb generation (albeit for large tooth spacing). Critical coupling was achieved, or nearly achieved, at all relevant wavelengths without incorporating sharp components in the first two cases. In particular, all features of the SHG system are larger than 120 nm. Our results continue the promising trend seen in application of inverse design to free-space and on-chip couplers, rectifiers, and multiplexers, indicating the potential of these techniques to enable significant improvements in integrated nonlinear photonics.

Funding

National Science Foundation under Grant No. DMR-1454836, Grant No. DMR 1420541, and Award EFMA-1640986; and the National Science and Research Council of Canada under PDF-502958-2017.

References

1. Z. Yu, "Fundamental limit of nanophotonic light trapping in solar cells," *Proc. Natl. Acad. Sci.* **107**, 17491 (2010).
2. O. D. Miller, S. G. Johnson, and A. W. Rodriguez, "Shape-independent limits to near-field radiative heat transfer," *Phys. Rev. Lett.* **115**, 204302 (2015).
3. A. Arabi and A. Faraon, "Fundamental limits of ultrathin metasurfaces," *Sci. Reports* **7** (2017).
4. C. Sitawarin, W. Jin, Z. Lin, and A. W. Rodriguez, "Inverse designed photonic fibers and metasurfaces for nonlinear frequency conversion," *arXiv:1711.07810* (2017).
5. Q. Li, M. Davanço, and K. Srinivasan, "Efficient and low-noise single-photon-level frequency conversion interfaces using silicon nanophotonics," *Nat. Photonics* **10**, 406–414 (2016).
6. D. Sell, J. Yang, S. Doshay, R. Yang, and J. A. Fan, "Large-angle, multifunctional metagratings based on freeform multimode geometries," *Nano Lett.* **17**, 3752–3757 (2017).
7. F. Callewaert, V. Velez, P. Kumar, A. Sahakian, and K. Aydin, "Inverse-designed broadband all-dielectric electromagnetic metadevices," *Sci. Reports* **8**, 1358 (2018).
8. W. Jin, R. Messina, and A. W. Rodriguez, "Overcoming limits to near-field radiative heat transfer in uniform planar media through multilayer optimization," *Opt. Express* **25**, 14746–14759 (2017).
9. W. Jin, S. Molesky, Z. Lin, and A. W. Rodriguez, "Material scaling and frequency-selective enhancement of near-field radiative heat transfer for lossy metals in two dimensions via inverse design," *arXiv:1802.05744* (2018).
10. D. A. Miller, "Silicon photonics: Meshing optics with applications," *Nat. Photonics* **11**, 403 (2017).
11. J. S. Jensen and O. Sigmund, "Topology optimization for nano-photonics," *Laser & Photonics Rev.* **5**, 308–321 (2011).
12. J. Lu and J. Vučković, "Nanophotonic computational design," *Opt. Express* **21**, 13351 – 13367 (2013).
13. C. M. Lalau-Keraly, S. Bhargava, O. D. Miller, and E. Yablonovitch, "Adjoint shape optimization applied to electromagnetic design," *Opt. Express* **21**, 21693 – 21701 (2013).
14. S. Molesky, Z. Lin, A. Y. Piggott, W. Jin, J. Vučković, and A. W. Rodriguez, "Outlook for inverse design in nanophotonics," *arXiv:1801.06715* (2018).
15. A. Rodriguez, M. Soljačić, J. D. Joannopoulos, and S. G. Johnson, " χ (2) and χ (3) harmonic generation at a critical power in inhomogeneous doubly resonant cavities," *Opt. Express* **15**, 7303–7318 (2007).
16. Z. Lin, X. Liang, M. Lončar, S. G. Johnson, and A. W. Rodriguez, "Cavity-enhanced second-harmonic generation via nonlinear-overlap optimization," *Optica* **3**, 233–238 (2016).
17. Z. Lin, M. Lončar, and A. W. Rodriguez, "Topology optimization of multi-track ring resonators and 2d microcavities for nonlinear frequency conversion," *Opt. Lett.* **42**, 2818–2821 (2017).
18. H. Chandralim, S. C. Rand, and X. Fan, "Evanescent coupling between refillable ring resonators and laser-inscribed optical waveguides," *Appl. Opt.* **56**, 4750–4756 (2017).
19. Y. A. Vlasov and S. J. McNab, "Losses in single-mode silicon-on-insulator strip waveguides and bends," *Opt. Express* **12**, 1622–1631 (2004).
20. T. Fujisawa, S. Makino, T. Sato, and K. Saitoh, "Low-loss, compact, and fabrication-tolerant si-wire 90° waveguide bend using clothoid and normal curves for large scale photonic integrated circuits," *Opt. Express* **25**, 9150–9159 (2017).
21. V. Donzella, S. T. Fard, and L. Chrostowski, "Study of waveguide crosstalk in silicon photonics integrated circuits," *Photonics North* **8915**, 89150Z (2013).
22. S. Jahani and Z. Jacob, "Photonic skin-depth engineering," *JOSA B* **32**, 1346–1353 (2015).
23. M. Ghebrebrhan, P. Bermel, Y. Yeng, I. Celanovic, M. Soljačić, and J. Joannopoulos, "Tailoring thermal emission via q matching of photonic crystal resonances," *Phys. Rev. A* **83**, 033810 (2011).
24. J. Wu, "Broadband light absorption by tapered metal-dielectric multilayered grating structures," *Opt. Commun.* **365**, 93–98 (2016).

25. Y. Lin, Y. Cui, F. Ding, K. H. Fung, T. Ji, D. Li, and Y. Hao, "Tungsten based anisotropic metamaterial as an ultra-broadband absorber," *Opt. Mater. Express* **7**, 606–617 (2017).
26. C. Argyropoulos, K. Q. Le, N. Mattiucci, G. D'Aguanno, and A. Alu, "Broadband absorbers and selective emitters based on plasmonic brewster metasurfaces," *Phys. Rev. B* **87**, 205112 (2013).
27. X. Liu, K. Fan, I. V. Shadrivov, and W. J. Padilla, "Experimental realization of a terahertz all-dielectric metasurface absorber," *Opt. Express* **25**, 191–201 (2017).
28. S. Molesky, C. J. Dewalt, and Z. Jacob, "High temperature epsilon-near-zero and epsilon-near-pole metamaterial emitters for thermophotovoltaics," *Opt. Express* **21**, A96–A110 (2013).
29. J. Rensberg, Y. Zhou, S. Richter, C. Wan, S. Zhang, P. Schöppe, R. Schmidt-Grund, S. Ramanathan, F. Capasso, M. A. Kats *et al.*, "Epsilon-near-zero substrate engineering for ultrathin-film perfect absorbers," *Phys. Rev. Appl.* **8**, 014009 (2017).
30. Y. Song, C. Wang, Y. Lou, B. Cao, and X. Li, "Near-perfect absorber with ultrawide bandwidth in infrared region using a periodically chirped structure," *Opt. Commun.* **305**, 212–216 (2013).
31. D. Ji, H. Song, X. Zeng, H. Hu, K. Liu, N. Zhang, and Q. Gan, "Broadband absorption engineering of hyperbolic metafilm patterns," *Sci. Reports* **4**, 4498 (2014).
32. V. Rinnerbauer, Y. Shen, J. D. Joannopoulos, M. Soljačić, F. Schäffler, and I. Celanovic, "Superlattice photonic crystal as broadband solar absorber for high temperature operation," *Opt. Express* **22**, A1895–A1906 (2014).
33. V. Ganapati, O. D. Miller, and E. Yablonovitch, "Light trapping textures designed by electromagnetic optimization for subwavelength thick solar cells," *IEEE J. Photovoltaics* **4**, 175–182 (2014).
34. S. Sui, H. Ma, J. Wang, Y. Pang, and S. Qu, "Topology optimization design of a lightweight ultra-broadband wide-angle resistance frequency selective surface absorber," *J. Phys. D: Appl. Phys.* **48**, 215101 (2015).
35. S. M. Fu, Y. K. Zhong, N. P. Ju, M.-H. Tu, B.-R. Chen, and A. Lin, "Broadband polarization-insensitive metamaterial perfect absorbers using topology optimization," *IEEE Photonics J.* **8**, 1–11 (2016).
36. V. R. Almeida, R. R. Panepucci, and M. Lipson, "Nanotaper for compact mode conversion," *Opt. Lett.* **28**, 1302–1304 (2003).
37. T. Carmon, S. Y. Wang, E. P. Ostby, and K. J. Vahala, "Wavelength-independent coupler from fiber to an on-chip cavity, demonstrated over an 850nm span," *Opt. Express* **15**, 7677–7681 (2007).
38. Y. Fu, T. Ye, W. Tang, and T. Chu, "Efficient adiabatic silicon-on-insulator waveguide taper," *Photonics Res.* **2**, A41–A44 (2014).
39. T. Tiecke, K. Nayak, J. Thompson, T. Peyronel, N. De Leon, V. Vuletić, and M. Lukin, "Efficient fiber-optical interface for nanophotonic devices," *Optica* **2**, 70–75 (2015).
40. A. C. Niederberger, D. A. Fattal, N. R. Gauger, S. Fan, and R. G. Beausoleil, "Sensitivity analysis and optimization of sub-wavelength optical gratings using adjoints," *Opt. Express* **22**, 12971–12981 (2014).
41. R. Mansoor, H. Sasse, and A. Duffy, "Optimization of reflection coefficient in ring resonator add/drop filters," *Int. J. Numer. Model. Electron. Networks, Devices Fields* **30** (2017).
42. L. Zhu, W. Yang, and C. Chang-Hasnain, "Very high efficiency optical coupler for silicon nanophotonic waveguide and single mode optical fiber," *Opt. Express* **25**, 18462–18473 (2017).
43. Z. Li, M.-H. Kim, C. Wang, Z. Han, S. Shrestha, A. C. Overvig, M. Lu, A. Stein, A. M. Agarwal, M. Lončar *et al.*, "Controlling propagation and coupling of waveguide modes using phase-gradient metasurfaces," *Nat. Nanotechnol.* **12**, 675 (2017).
44. J. Li, Y. Liu, Y. Meng, K. Xu, J. Du, F. Wang, Z. He, and Q. Song, "2- μ m wavelength grating coupler, bent waveguide and tunable microring on silicon photonic mpw," *IEEE Photonics Technol. Lett.* (2018).
45. X. Jiang, L. Shao, S.-X. Zhang, X. Yi, J. Wiersig, L. Wang, Q. Gong, M. Lončar, L. Yang, and Y.-F. Xiao, "Chaos-assisted broadband momentum transformation in optical microresonators," *Science* **358**, 344–347 (2017).
46. A. Y. Piggott, J. Lu, K. G. Lagoudakis, J. Petykiewicz, T. M. Babinec, and J. Vučković, "Inverse design and demonstration of a compact and broadband on-chip wavelength demultiplexer," *Nat. Photonics* **9**, 374–377 (2015).
47. L. F. Frellsen, Y. Ding, O. Sigmund, and L. H. Frandsen, "Topology optimized mode multiplexing in silicon-on-insulator photonic wire waveguides," *Opt. Express* **24**, 16866–16873 (2016).
48. X. Liang and S. G. Johnson, "Formulation for scalable optimization of microcavities via the frequency-averaged local density of states," *Opt. Express* **21**, 30812–30841 (2013).
49. F. Wang, B. S. Lazarov, and O. Sigmund, "On projection methods, convergence and robust formulations in topology optimization," *Struct. Multidiscip. Optim.* **43**, 767–784 (2011).
50. Y. K. Chembo and N. Yu, "Modal expansion approach to optical-frequency-comb generation with monolithic whispering-gallery-mode resonators," *Phys. Rev. A* **82**, 033801 (2010).
51. X. Guo, C.-L. Zou, H. Jung, and H. X. Tang, "On-chip strong coupling and efficient frequency conversion between telecom and visible optical modes," *Phys. Rev. Lett.* **117**, 123902 (2016).
52. M. H. Pfeiffer, J. Liu, M. Geiselmann, and T. J. Kippenberg, "Coupling ideality of integrated planar high-q microresonators," *Phys. Rev. Appl.* **7**, 024026 (2017).
53. W. Suh, Z. Wang, and S. Fan, "Temporal coupled-mode theory and the presence of non-orthogonal modes in lossless multimode cavities," *IEEE J. Quantum Electron.* **40**, 1511–1518 (2004).
54. M. L. Gorodetsky and V. S. Ilchenko, "Optical microsphere resonators: optimal coupling to high-q whispering-gallery modes," *JOSA B* **16**, 147–154 (1999).
55. Z.-F. Bi, A. W. Rodriguez, H. Hashemi, D. Duchesne, M. Loncar, K.-M. Wang, and S. G. Johnson, "High-efficiency

- second-harmonic generation in doubly-resonant $\chi^{(2)}$ microring resonators,” Opt. Express **20**, 7526–7543 (2012).
56. Q. Xu, D. Fattal, and R. G. Beausoleil, “Silicon microring resonators with 1.5- μm radius,” Opt. Express **16**, 4309–4315 (2008).